

RESEARCH

Open Access



A novel tri-mode detection platform for ampicillin and drug resistance genes by CRISPR-driven luminescent nanozymes

Tao Zhang^{1,2}, Guiling Liu^{1,2}, Siwei Sun³, Zongwu Meng^{1,2}, Yuzhe Qiu^{1,2} and Ping Ding^{1,2*}

Abstract

The antibiotic residues pose significant risks for bacterial resistance. To address the practical requirements for rapid, accurate, and on-site detection of antibiotic residues and monitoring the abundance of associated resistance genes, we report a smartphone-integrated multi-mode platform. The platform is aimed to simultaneous, accurate, and visual quantitative detection of ampicillin (AMP) and β -lactam antibiotic resistance genes (*blaTEM*). Specifically, we developed a magnetically controlled fluorescence, colorimetric, and photothermal biosensor based on a magnetic separation unit (aminated modified complementary DNA chain (NH₂-cDNA) loading on the surface of Ferrosioferric Oxide@polydopamine (Fe₃O₄@PDA, FP), FP@cDNA) and a signal unit (the aptamer nucleic acid chain modified by phosphate group linked to Prussian blue@UiO-66@manganese dioxide (PB@UiO-66@MnO₂, PUM) through Zr-O-P bond, PUM@Apt), for the integrated detection of AMP and *blaTEM*. By utilizing complementary base pairing between FP@cDNA and PUM@Apt, along with precise aptamer recognition the AMP, we achieved the fluorescence quantitative detection of AMP by measuring the signal unit in the supernatant. Subsequently, the difference of signal units in colorimetric process leads to a varying conversion rate of oxidized 3,3',5,5'-Tetramethylbenzidine (oxTMB), enabling the output of colorimetric and photothermal signals. The competitive binding of aptamers permitting the determination of AMP in the range of 0–160 pM with a low detection limit (0.34 pM). Additionally, in the presence of *blaTEM*, the activated CRISPR/Cas12a indiscriminately cleaves the single-stranded portion of the FP@DNA@PUM complex obtained by magnetic separation. A PUM-based three-signal detection scheme was established for the sensitive determination of *blaTEM* with the limit of detection (LOD) of 1.03 pM. The integration of smartphone-assisted analysis broadens the potential of the platform for visual detection. Notably, the innovative platform, with its excellent stability, exhibits great potential as a simple yet robust approach for the simultaneously visually monitoring antibiotics and drug resistance genes, and holds promise in the field of kit development.

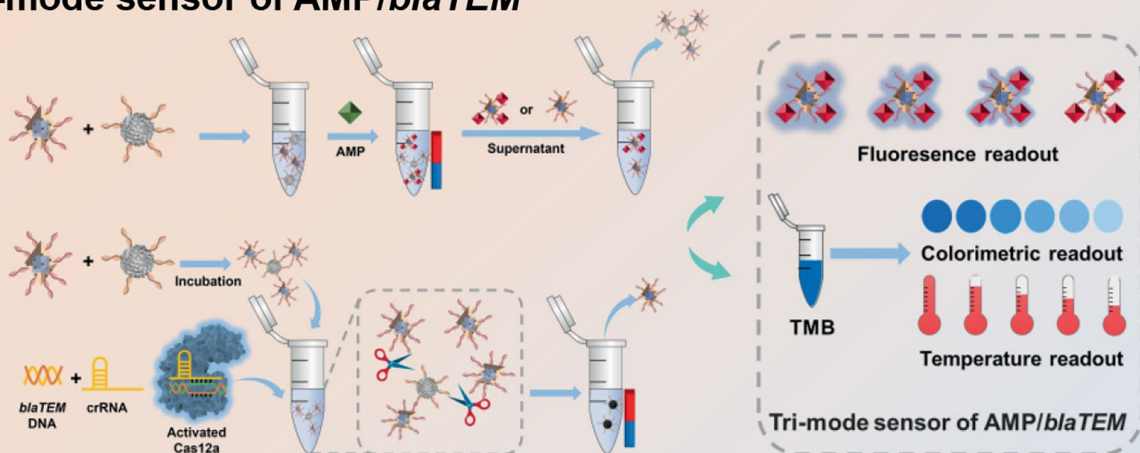
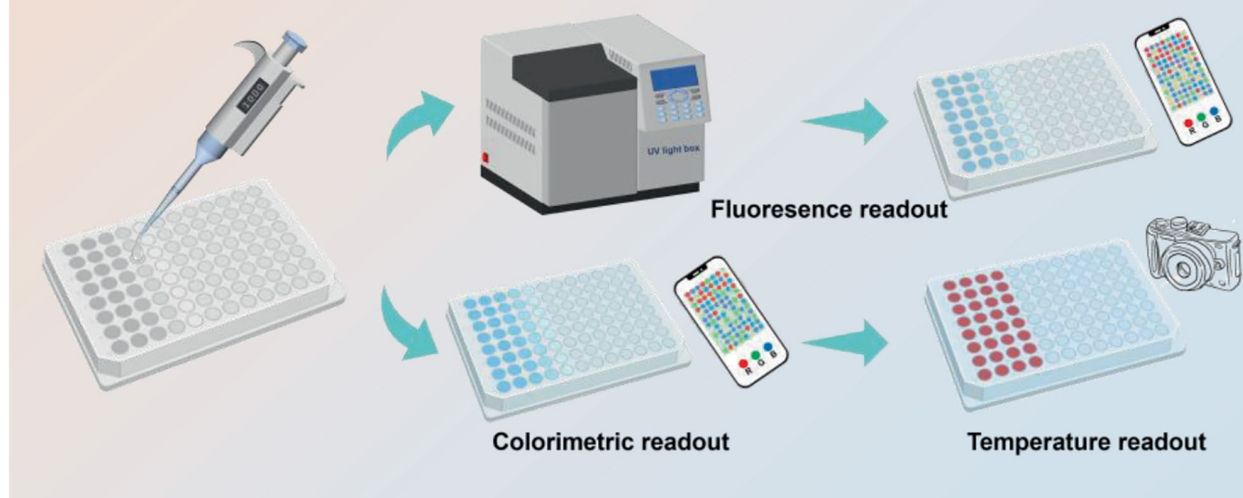
*Correspondence:

Ping Ding
Pingshui@csu.edu.cn

Full list of author information is available at the end of the article



© The Author(s) 2025. **Open Access** This article is licensed under a Creative Commons Attribution-NonCommercial-NoDerivatives 4.0 International License, which permits any non-commercial use, sharing, distribution and reproduction in any medium or format, as long as you give appropriate credit to the original author(s) and the source, provide a link to the Creative Commons licence, and indicate if you modified the licensed material. You do not have permission under this licence to share adapted material derived from this article or parts of it. The images or other third party material in this article are included in the article's Creative Commons licence, unless indicated otherwise in a credit line to the material. If material is not included in the article's Creative Commons licence and your intended use is not permitted by statutory regulation or exceeds the permitted use, you will need to obtain permission directly from the copyright holder. To view a copy of this licence, visit <http://creativecommons.org/licenses/by-nc-nd/4.0/>.

Graphical Abstract**Tri-mode sensor of AMP/*bla*TEM****Visual detection of AMP/*bla*TEM**

Keywords Ampicillin, *Bla*TEM, Aptamer, CRISPR/Cas12a, Tri-mode detection, Visual detection

Introduction

The remarkable antimicrobial effectiveness of penicillin has driven the widespread application in aquaculture, animal husbandry, clinical medicine, and other fields [1, 2]. However, the excessive application of antibiotics in recent decades has resulted in significant pollution of the water environment [3]. Chronic human exposure to these residues via direct ingestion or environmental vectors can lead to bioaccumulation, eliciting progressive adverse health consequences [4]. Furthermore, while the antibiotic resistance genes (ARGs) inherent in nature are

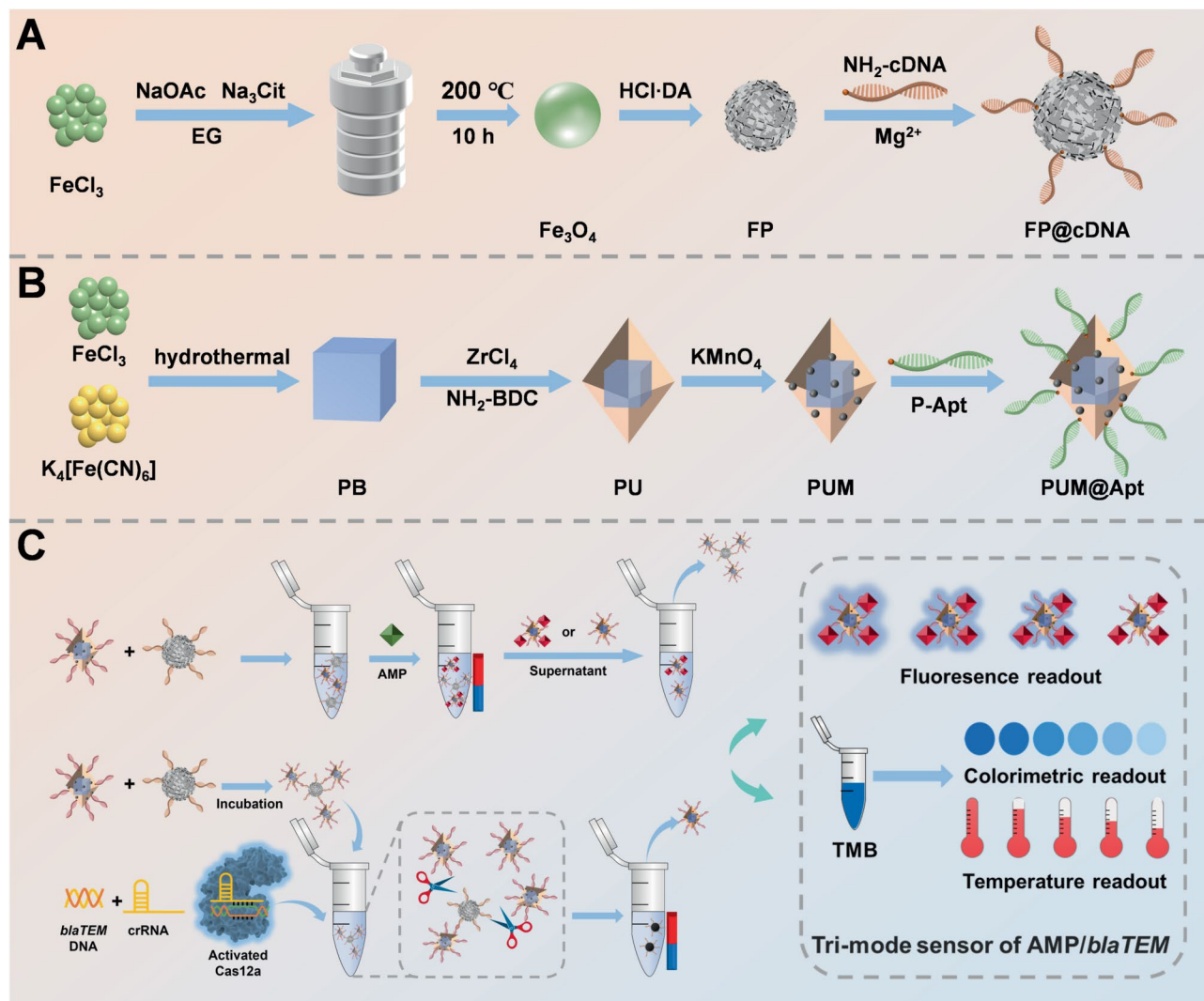
not directly related to human activities, the extensive use of antibiotics creates a selective environment that favoring bacteria with drug resistance traits, thereby increasing resistance gene reservoirs in ecological systems [5]. Specialized environments, such as hospitals, exhibit high levels of antibiotics and drug resistance genes. Consequently, integrated detection strategies for simultaneous quantification of antibiotic and ARGs provide vital insights for guiding clinical decision-making and predicting the development trend of drug resistance. To achieve the above purpose, developing a convenient, rapid, highly

selective, and highly sensitive detection approach for antibiotics and drug resistance genes is undoubtedly a top priority.

AMP, a key member of the β -lactam antibiotics family, plays a crucial role in managing of bacterial infections [6]. As a semisynthetic penicillin derivative, it exerts through β -lactam ring-mediated irreversible inhibition of bacterial cell wall transpeptidases [7, 8]. However, since the 1960s, the widespread clinical use has led to serious consequences of bacterial resistance to β -lactam antibiotics [9]. Among these, the emergence of TEM-type β -lactamases (encoded by the *blaTEM*) presents a major challenge in the field of β -lactam therapy [10]. The TEM-type β -lactamases are capable of hydrolysing the β -lactam ring of AMP with remarkable catalytic efficiency, thereby rendering the antibiotics ineffective [11]. Notably, *blaTEM* variants account for over 60% of bacterial AMP resistance in Enterobacteriaceae. Meanwhile, *blaTEM* exacerbates the spread of resistance through horizontal transfer between microbial communities via plasmids and transposons, especially in agricultural and aquatic environments where AMP residues persist. Consequently, detecting AMP residues in ecological systems and assessing the levels of the *blaTEM* are highly significant. Currently, the conventional antibiotic detection mainly relies on high-performance liquid chromatography (HPLC) and Enzyme-Linked Immunosorbent Assay (ELISA) [12, 13]. However, these methods tend to involve bulky and sophisticated instrumentation, time-consuming operations, and exhibit low sensitivity in the detection process [14]. Simultaneously, conventional ARGs detection via real-time fluorescence quantitative Polymerase Chain Reaction (RT-qPCR) and metagenomic sequencing suffers from high costs and prolonged turnaround times, hindering environmental and clinical applications [15, 16]. Aptamer, characterized by a distinct nucleotide sequence, uses its unique three-dimensional conformation to bind with high specificity and affinity to its target, facilitating effective detection [17]. By accurately identifying the target, Clustered Regularly Interspaced Short Palindromic Repeats (CRISPR) technology activates the trans-cleavage activity of the Cas protein, while the cleavage of single-stranded nucleic acids increases the signal output, thereby improving detection sensitivity [18, 19]. Despite these advancements, the integration of aptamer-mediated small-molecule detection with CRISPR-based gene analysis for simultaneous antibiotic-ARGs quantification remains unexplored in environmental biosensing. The dual quantification of AMP residues and *blaTEM* has significant implications: (1) Clinically: it enables real-time drug resistance analysis to guide antibiotic management; (2) Environmentally: it provides early warning of pollution levels and the development of drug resistance genes through long-term monitoring of sewage.

In biosensor signal transduction systems, the colorimetric detection has emerged as a preeminent modality due to its operational simplicity and rapid signal interpretation [20]. However, the recognition of a single colorimetric signal lacks precision due to its limited sensitivity, vulnerability to external interference, and various influencing factors [21, 22]. Moreover, compared to natural enzymes that require stringent reaction conditions, synthetic nanozymes are increasingly favored as superior signal transducers owing to their abundant sourcing, cost-effectiveness, tunable catalytic properties, and exceptional environmental resilience [23, 24]. The strategic integration of fluorescence, colorimetric, and photothermal functionalities presents transformative opportunities for biosensing. The enhanced sensitivity of fluorescence, combined with the easy operation and reading of photothermal signals, significantly complements the limitations of the single colorimetric method. The interdependent correction mechanism between the signals of the three different modes substantially boosts the reliability of the sensor [25, 26]. Consequently, the development of a rapid and convenient multi-signal integrated sensor for the simultaneous detection of antibiotics and drug resistance genes represents a highly effective approach.

Considering the above requirements, we designed a tri-mode sensing platform that integrates fluorescence, colorimetric, and photothermal modalities, combining aptamer recognition and CRISPR/Cas12a trans-cleavage for the simultaneous visual detection of AMP and *blaTEM* (Scheme 1). Initially, FP magnetic nanoparticles were functionalized with NH_2 -cDNA via Michael addition/Schiff base reactions, constructing the magnetic separation unit (FP@cDNA). Subsequently, the luminescent nanozyme (PUM), exhibiting excellent fluorescence and peroxidase (POD) activity, was covalently conjugated to phosphoric group modified aptamer (P-Apt) to develop PUM@Apt through the formation of Zr-O-P bonds. Therefore, capitalizing on the specific recognition mechanism of the aptamer and the competitive binding principle of aptamer and cDNA, the FP@cDNA was employed to achieve superparamagnetic isolation of residual PUM@Apt remaining in the supernatant after AMP binding by base complementary pairing. The strategy established a fluorescence-colorimetric dual-mode quantitative detection system for AMP by detecting the concentration of residual PUM@Apt in the supernatant. Furthermore, tri-mode detection of AMP was accomplished by exploiting the temperature difference formed by the difference of oxTMB, the chromogenic product of colorimetric process, irradiated by 808 nm near-infrared laser. Significantly, in the presence of *blaTEM*, it specifically binds to CRISPR RNA (crRNA), activating the single-stranded DNA cleavage activity of CRISPR/



Scheme 1 (A) Schematic representation of the preparation of FP@cDNA. (B) Schematic representation of the preparation of PUM@Apt. (C) Schematic of tri-mode detection of AMP and *blaTEM*

Cas 12a. This enzymatic process unrestrictedly cuts the single-stranded region of the FP@DNA@PUM complex isolated from AMP detection. Subsequent secondary magnetic separation enabled precise quantification of PUM released in the supernatant, thereby establishing an integrated fluorescence/colorimetric/photothermal tri-mode detection platform for *blaTEM*. To meet the actual requirements of rapid and on-site visual detection, smartphones were further integrated into the program of the composite sensing platform, enabling simultaneous, accurate, and visual quantitative detection of AMP and *blaTEM*. This strategy demonstrates significant potential in the field of monitoring the abundance of antibiotics and drug resistance genes. Moreover, the modular design of platform permits rapid adaptation for detection of diverse antibiotics and associated resistance genes

through sequence-specific reprogramming recognition elements of cDNA probes and aptamer.

Experimental section

Reagents and chemicals

N, N-dimethylformamide (DMF), citric acid (CA), zirconium chloride ($ZrCl_4$), 2-aminoterephthalic acid (NH_2 -BDC), absolute alcohol (EtOH), acetic acid (HAc), anhydrous sodium acetate (NaAc), trometamol (Tris), trisodium citrate dihydrate, ethylene glycol, amoxicillin (AMX), chlortetracycline (CTC), erythromycin (ERY), kanamycin (KAN), sulfamethoxazole (SMX), sulfamethazine (SMZ), ampicillin (AMP), dopamine hydrochloride (DA-HCl), magnesium chloride ($MgCl_2$), sodium chloride (NaCl), EDTA disodium salt dihydrate (EDTA-2Na), polysorbate 20 (Tween 20), nuclease-free water and 6×loading buffer were purchased from Adamas-beta

Reagent Co., Ltd. (Shanghai, China). Tetracycline (TC), oxytetracycline (OTC), ferric chloride hexahydrate ($\text{FeCl}_3 \cdot 6\text{H}_2\text{O}$) and 3,3',5,5'-tetramethylbenzidine (TMB) were purchased from Aladdin Biochemical Technology Co., Ltd. (Shanghai, China). Hydrochloric acid (HCl), hydrogen peroxide (H_2O_2 , 30%) and potassium permanganate (KMnO_4) were purchased from Sinopharm Chemical Reagent Co., Ltd. (Shanghai, China). Tetrapotassium hexacyanoferrate trihydrate ($\text{K}_4[\text{Fe}(\text{CN})_6]$) was purchased from Tianjin Guangfu Technology Development Co., Ltd. (Tianjin, China). Penicillin G (PG) was purchased from Dingguo Changsheng Biotechnology Co., Ltd. (Beijing, China). LbCas12a enzyme and 10 \times NEB buffer were sourced from New England Biolabs (USA). DNA markers (20–200 bp) were ordered from Takara Biotech, Inc. (Dalian, China). Acrylamide/bis-acrylamide 30% solution (29:1) was purchased from Beijing Boao Sen Biotechnology Co., Ltd. (Beijing, China). Super GelBlue nucleic acid dye was acquired from UElandy Co., Ltd. (Suzhou, China). DNA sequences were purchased from Sangon Biotech Co., Ltd. (Shanghai, China). The crRNA was synthesized by GenScript (Nanjing, China). The sequences used in the experiment are provided in Table S5. All reagents were of analytical grade, and deionized water was used throughout the experiment.

Preparation of magnetic separation unit

Synthesis of the Fe_3O_4 @PDA core-shell nanoparticles

Typically, $\text{FeCl}_3 \cdot 6\text{H}_2\text{O}$ (1.08 g, 4.0 mmol) and trisodium citrate dihydrate (0.27 g, 0.68 mmol) were first dissolved in ethylene glycol (20 mL). Afterward, sodium acetate (1.20 g) was added with stirring. The mixture was stirred vigorously for 30 min and then sealed in a poly(tetrafluoroethylene)-lined stainless-steel autoclave (50 mL capacity). The autoclave was heated at 200 °C and maintained for 10 h, after which it was allowed to cool to room temperature. The black products were washed with ethanol and deionized water for several times. To synthesize Fe_3O_4 @PDA, 20.0 mg of as-prepared Fe_3O_4 NPs were dispersed in 50.0 mL of 10.0 mM Tris-HCl buffer containing 2.0 mg/mL DA-HCl (pH 8.5). The mixed solution was allowed to proceed for 40 min under ultrasound (40 kHz) with binding force. Continuous mechanical stirring was conducted for 12 h at room temperature. The resulting product was collected and washed with deionized water and dried under vacuum overnight.

Synthesis of FP@cDNA

NH_2 -cDNA molecules (5 nmol) were mixed with Fe_3O_4 @PDA (1 mg) in 1 mL of Tris-HCl buffer (10 mM, pH 8.5) containing 150 mM NaCl and 20 mM MgCl_2 . The mixtures were reacted at room temperature for 10 h under shaking. Covalent attachment of NH_2 -cDNA onto Fe_3O_4 @PDA was achieved via Michael addition/Schiff

base reactions. The resulting FP@cDNA conjugates were washed three times with a TE solution (10 mM Tris-HCl, 5 mM EDTA, pH 8.5) for 20 min each time to remove unreacted NH_2 -cDNA. Subsequently, the FP@cDNA conjugates were dispersed in 1 mL of Tris-HCl buffer and stored at 4 °C for future use.

Construction of signal unit

Synthesis of Prussian blue nanoparticles (PB)

$\text{FeCl}_3 \cdot 6\text{H}_2\text{O}$ (5.3 mg) and CA (107 mg) were added to 20 mL of deionized water. Then, 20 mL of deionized water deionized water containing $\text{K}_4[\text{Fe}(\text{CN})_6]$ (8.4 mg) and CA (107 mg) was added dropwise into the above solution under vigorous stirring at 60 °C. A bright blue color rapidly appeared during the blending process. The reaction was maintained for 5 min and cooled down to 20 °C for another 30 min. The PB NPs precipitation was obtained by centrifugation (12000 rpm, 30 min) three times with ethanol after the reaction. Finally, the obtained precipitation was dried overnight under vacuum at room temperature.

Synthesis of PB@UiO-66 (PU)

For the preparation of PB@UiO-66, 10 mg of PB NPs was added to 10 mL of DMF and ultrasonicated for 30 min. The resulting dispersion was added to 8 mL of DMF which contained 37.5 mg of ZrCl_4 , and 31.6 mg of NH_2 -BDC under the sonicated condition for 30 min. The mixture was sealed in a Teflon-lined stainless-steel reactor with a temperature of 120 °C for 24 h. The resulting PB@UiO-66 was washed three times with DMF and anhydrous ethanol, after which the solid was vacuum-dried at 60 °C overnight.

Synthesis of PB@UiO-66@ MnO_2 (PUM)

Specifically, 10 mg of PB@UiO-66 was washed three times with deionized water and subsequently resuspended in 2 mL of deionized water. An aqueous solution of KMnO_4 (2 mL, 1 mg/mL) was then added to the PB@UiO-66 aqueous suspension. The mixture was vigorously stirred at room temperature for 30 min, followed by three washes with deionized water and resuspension in 2 mL of deionized water.

Construction of PUM@Apt

Briefly, 100 μL of P-Apt (10 μM) was added to 1 mL of PUM (1 mg/mL), which was then incubated in a metal bath at 37 °C, 1200 rpm for 1.5 h. After centrifugation at 8000 rpm for 10 min, the supernatant was discarded and washed three times with ultrapure water to obtain the PUM@Apt.

Construction of FP@DNA@PUM probe

PUM@Apt was thoroughly mixed with 1 mL of Tris-HCl coupling buffer (10 mM, pH 8.5) containing 1 mg of FP@cDNA, 150 mM NaCl, and 20 mM MgCl₂. The mixture was then subjected to continuous shaking for 2 h at room temperature to facilitate the reaction. Upon completion of the reaction, the resultant product, FP@DNA@PUM, was isolated through magnetic separation. The isolated product was subsequently washed multiple times with Tris-HCl buffer to remove any unreacted components or impurities. Finally, the purified FP@DNA@PUM was resuspended in 1 mL of ultrapure water and stored at 4 °C for future use.

Sensing procedure

Fluorescence, colorimetric and photothermal detection of AMP

FP@cDNA and PUM@Apt were used for AMP detection. Specifically, a mixture of 300 µL of binding buffer (10 mM Tris-HCl, 1 M NaCl, 6 mM CaCl₂, 0.02% Tween 20, pH 7.0), 50 µL of PUM@Apt (300 µg/mL), and 75 µL of varying concentrations of AMP was oscillated at a constant temperature of 37 °C for 10 min. Then, 75 µL of FP@cDNA (1 mg/mL) was added, and the mixture was further incubated for 40 min to capture uncombined PUM@Apt. After magnetic separation, the supernatants were collected for fluorescence measurements. The excitation wavelength was 330 nm and fluorescence spectra were collected from 380 to 600 nm. Subsequently, 500 µL of acetate-sodium acetate buffer (HAC-NaAc, 10 mM, pH 4.0) containing 5 mM H₂O₂ and 0.5 mM TMB was added. After 10 min of incubation at room temperature, the results were quantitatively analyzed using an Ultraviolet-visible Spectrophotometer (UV-vis). For photothermal analysis, the resulting solution (0.5 mL) was added to a 600 µL centrifuge tube, then irradiated with 808 nm laser for 5 min. The temperatures were recorded and the photothermal signals of the solution were recorded with an infrared thermal camera. In order to ensure reproducibility and reliability, all experiments were conducted with at least three duplicates.

For fluorescence visual detection of AMP, the supernatants were added to the 24-well plates, placed in a 302 nm ultraviolet light box, and images were captured using a smartphone. The RGB (Red, Green, Blue) values were measured using mobile phone software (Color Grab). A standard curve correlating chromatic values to antibiotic concentration was established for the quantitative detection of AMP. For the colorimetric visualization detection of AMP, the supernatants were added to the 24-well plates with 500 µL of acetate-sodium acetate buffer (HAC-NaAc, 10 mM, pH 4.0) containing 5 mM H₂O₂ and 0.5 mM TMB, images were captured using a smartphone, and the RGB values were identified by the mobile

phone software (Color Grab). A standard curve was then established to correlate chromatic values with AMP concentrations for quantitative detection. For photothermal visual detection purposes, the oxTMB solution was irradiated with an 808 nm laser for 5 min. The resulting temperature changes (ΔT) were monitored using an infrared thermal imager, and a correlation between ΔT values and AMP concentration could be established.

Fluorescence, colorimetric and photothermal detection of blaTEM

For the approach, the CRISPR/Cas12a system was composed of 2 µL of Cas12a (1 µM), 2 µL of crRNA (1 µM), 2 µL of varying concentrations of *blaTEM*, 2 µL of reaction buffer (10×NEB buffer r2.1), and 12 µL of nuclease-free water. After incubated at 37 °C for 10 min, 20 µL of a 2 mg/mL FP@DNA@PUM signaling probe was added to reaction system. The reaction proceeded at 37 °C and shaking speed of the oscillator was 1000 rpm for 2 h. Following this, the supernatant was separated via magnetic separation. Then the supernatants were collected for fluorescence measurements. Subsequently, 460 µL of acetate-sodium acetate buffer (HAC-NaAc, 10 mM, pH 4.0) containing 5 mM H₂O₂ and 0.5 mM TMB was added. After 10 min of incubation at 37 °C, the results were quantitatively analyzed using a UV-vis. For photothermal analysis, the resulting solution was added to a 600 µL centrifuge tube, then irradiated with 808 nm laser for 5 min. The temperatures were recorded and the photothermal signals of the solution were recorded with an infrared thermal camera.

For fluorescence visual detection of *blaTEM*, the supernatants were added to the 24-well plates. Placed in a 302 nm ultraviolet light box, and images were captured using a smartphone. The RGB (Red, Green, Blue) values were measured using mobile phone software (Color Grab). For the colorimetric visualization detection of *blaTEM*, the supernatants were added to the 24-well plates with 460 µL of acetate-sodium acetate buffer (HAC-NaAc, 10 mM, pH 4.0) containing 5 mM H₂O₂ and 0.5 mM TMB, images were captured using a smartphone, and the RGB values were identified by the mobile phone software (Color Grab). For photothermal visual detection purposes, the oxTMB solution was irradiated with an 808 nm laser for 5 min. The resulting temperature changes (ΔT) were monitored using an infrared thermal imager, and a correlation between ΔT values and *blaTEM* concentration could be established.

Selectivity studies

In accordance with the established experimental protocol of the previously described sensing procedure, antibiotics with a concentration of 1 nM were utilized as interfering substances for selective test. Additionally, for the

selective assessment of *blaTEM*, interference genes at a concentration of 25 nM were employed. Meanwhile, ampicillin at a concentration of 160 pM and antibiotics at a concentration of 1 nM were introduced into the sensing system as target analytes. The anti-interference capability of the sensor system towards these antibiotics was evaluated by following the aforementioned experimental procedures. Furthermore, to assess the anti-interference capability specific to drug resistance genes, an interference gene at a concentration of 25 nM and the *blaTEM* at a concentration of 12.5 nM were utilized as the targets for detection, in accordance with the analytical methodology outlined within the sensing program.

Real sample analysis

Environmental water samples were collected from Xiangjiang River. For AMP analysis, water samples spiked with AMP (10 pM, 80 pM, 150 pM), then the solution were filtered through a 0.22 μm membrane filter. The filtered solution was then analyzed using an aptamer-based tri-mode biosensor for AMP. To conduct the *blaTEM* assay, *Pseudomonas aeruginosa* was selected as the test object. The RNA of *Pseudomonas aeruginosa* was

extracted and reverse transcribed using a kit. To assess the recovery of target genes individually, *blaTEM* was added to *Pseudomonas aeruginosa* samples. Samples spiked with *blaTEM* (50 pM, 500 pM, 1000 pM) were directly used for the subsequent CRISPR/Cas12a-based fluorescent, colorimetric, and photothermal detection.

Results and discussion

Synthesis and characterizations of FP and PUM

Schemes 1 provide a detailed illustrate the fabrication procedure of the magnetic separation unit and the signal unit. The morphologies of Fe_3O_4 and FP were observed using transmission electron microscopy (TEM). Figure 1A reveals that Fe_3O_4 exhibits a spherical morphology with a size of about 155 nm. Subsequently, dopamine self-polymerization generated a conformal polydopamine (PDA) coating (~ 50 nm thickness) on Fe_3O_4 surfaces, forming FP (Fig. 1B). Furthermore, the Zeta potential analysis revealed a significant charge shift from -13.28 mV for Fe_3O_4 to -4.42 mV for FP (Fig. 1C), confirming successful surface functionalization. Currently, the Vibrating sample magnetometry (VSM) indicates that the Fe_3O_4 exhibits significant magnetic properties [27], while

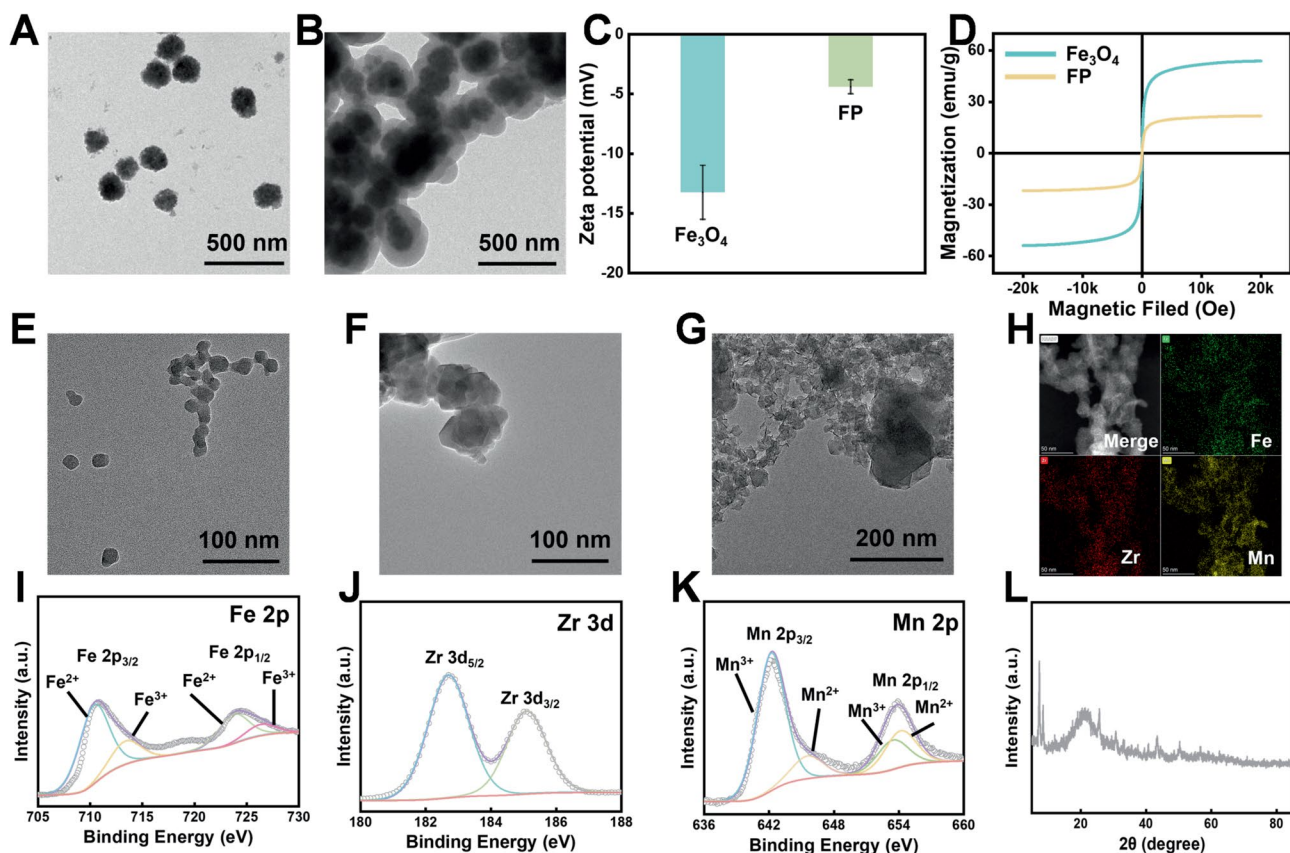


Fig. 1 (A) TEM images of Fe_3O_4 . (B) TEM images of FP. (C) Zeta potential of Fe_3O_4 and FP. (D) VSM of Fe_3O_4 and FP. (E) TEM image of PB. (F) TEM image of PU. (G) TEM image of PUM. (H) Fe, Zr and Mn element mapping for PUM. (I) Fe 2p XPS spectrum of PUM. (J) Zr 3d XPS spectrum of PUM. (K) Mn 2p XPS spectrum of PUM. (L) XRD spectrum of PUM

the modified FP also demonstrate robust magnetism (Fig. 1D). Magnetic separation demonstrated that Fe_3O_4 and FP could be efficiently separated within 30 s under the influence of an external magnetic field (Figure S1). Simultaneously, the structural evolution of Prussian blue (PB) to PUM nanocomposites were investigated using TEM. The structure of the PB exhibited a nanocube form characterized by extremely small dimensions (Fig. 1E). Following the in-situ synthesis of UiO-66 on the surface of PB, the PU displayed a prominent UiO-66 layer and underwent a substantial increase in size (Fig. 1F). Afterward, the formation of manganese dioxide (MnO_2) was observed on the outer layer of PU. TEM illustrated that flake MnO_2 was present on the surface of PUM (Fig. 1G). Moreover, PUM showed a uniform distribution of Fe, Zr, and Mn elements in the elemental mapping images (Fig. 1H).

The composition and valence states of elements on the surface of PUM were investigated using X-ray photoelectron spectroscopy (XPS). The survey spectra for PUM confirmed the presence of Fe, Zr, and Mn elements, corresponding to Fe 2p, Zr 3d, and Mn 2p, respectively, which is consistent with the elemental mapping images obtained by TEM (Figure S2). The high-resolution spectrum of Fe 2p revealed distinct peaks at 710.68 eV and 724.08 eV, corresponding to the Fe $2p_{3/2}$ and Fe $2p_{1/2}$ states, respectively (Fig. 1I) [28]. Furthermore, the Fe 2p spectrum was fitted into four peaks at 710.48, 713.58, 723.88 and 726.68 eV, respectively. Among them, the peaks at 710.48 eV and 723.88 eV correspond to Fe^{2+} , while the peaks at 713.58 eV and 726.68 eV are associated with Fe^{3+} [29]. The high-resolution spectra of Zr 3d were deconvoluted into two major peaks at 182.7 eV and 185.1 eV, which are attributed to Zr $3d_{5/2}$ and Zr $3d_{3/2}$, respectively (Fig. 1J) [30]. The XPS spectra of Mn 2p (Fig. 1K) showed the coexistence of Mn $2p_{3/2}$ (642.3 eV) and Mn $2p_{1/2}$ (653.7 eV) [31]. Meanwhile, the X-ray diffraction patterns (XRD) show that the diffraction peaks at 17.52° , 25.72° , 35.6° , 39.52° , 43.44° , 50.32° , 54.88° , 56.72° and 70.96° are well matched with the (200), (220), (400), (420), (422), (440), (600), (620) and (642) planes of PB lattice (JCPDS No. 52–1907) [32]. In addition, the XRD pattern exhibits diffraction peaks at angles of 7.4° , 8.5° , 14.8° , 17.1° , 22.3° , 25.7° , and 30.8° , which correspond to the (111), (200), (222), (400), (511), (600), and (711) crystal planes of UiO-66, respectively (Fig. 1L) [33]. Moreover, the pattern illustrated four diffraction peaks at approximately 16.32° , 25.72° , 37.52° , and 66.12° , which were indexed to the (002), (003), (100), and (110) planes of MnO_2 nanosheets [34]. The analysis reveals that the synthesis process of PUM has no influence the lattice structure of PB, UiO-66, and MnO_2 . Finally, Fourier transform infrared spectroscopy (FT-IR) was employed to record the changes in functional groups on the surface of the

material. The FT-IR results for PUM are shown in Figure S3. The absorption peaks at 510 cm^{-1} , 567 cm^{-1} , and 659 cm^{-1} are attributed to the formation of Mn-O, Fe-O, and Zr-O bonds, respectively [34, 35]. These results demonstrate the successful construction of FP and PUM.

FP and PUM Preparation and tri-mode sensor feasibility

Utilizing the dual mechanisms of aptamer-substrate specificity and base pairing, we established a simultaneous detection of AMP in the environment and the *bla-TEM* in *Pseudomonas aeruginosa*. Initially, to confirm the interaction between the aptamer and cDNA for effective magnetic separation, the feasibility of the DNA design was assessed using a 12% native polyacrylamide gel electrophoresis (PAGE) gel. As shown in Fig. 2A, the bands in lanes 2 and 3 correspond to the cDNA and aptamer, respectively. However, the binding band has obvious hysteresis in the presence of both (lane 4). Moreover, the combination of cDNA and aptamers under AMP conditions produced not only binding bands but also a population of free aptamers (lane 5) [36–38]. The result demonstrates the feasibility of DNA design based on competitive detection of AMP by cDNA and aptamer. Furthermore, the NH_2 -cDNA was connected with the dopamine layer containing catechol groups through the Michael addition/Schiff base reaction to construct the magnetic separation unit [39–41]. Fig. 2B illustrates that the fluorescence intensity in the supernatant experienced a notable reduction when FP@cDNA interacted with the Fluorescein Amidite-modified aptamer (Apt-FAM), while the fluorescence quenching effect of FP on FAM was nearly negligible. However, electrostatic repulsion between negatively charged DNA and the PDA layer limited surface conjugation efficiency [36]. To optimize the detection performance, critical parameters (Mg^{2+} concentration, NH_2 -cDNA concentration, coupling time, pH) were systematically evaluated. The data presented in Figure S4 indicate that the optimal conditions for constructing the magnetic separation unit were achieved after 10 h of using a Tris-HCl buffer (pH 8.5), containing 20 mM Mg^{2+} and 5 mM NH_2 -cDNA. In addition, after incubation with PUM, the UV-vis characteristic peak of Apt at 260 nm decreased significantly (Fig. 2C) [42]. Meanwhile, the magnetic separation unit and the signal unit exhibited a notably negative Zeta potential compared to FP and PUM, thereby confirming the effective attachment of cDNA and Apt to the surfaces of FP and PUM, respectively (Fig. 2D). These results collectively confirm the successful construction of the magnetic separation unit and signal unit.

The PUM nanozyme serves as a multifunctional signal molecule, exhibiting excellent fluorescence emission characteristics ($\text{Ex}/\text{Em}=330/450\text{ nm}$) and exceptional POD activity (Fig. 2E and 2F). Electron paramagnetic

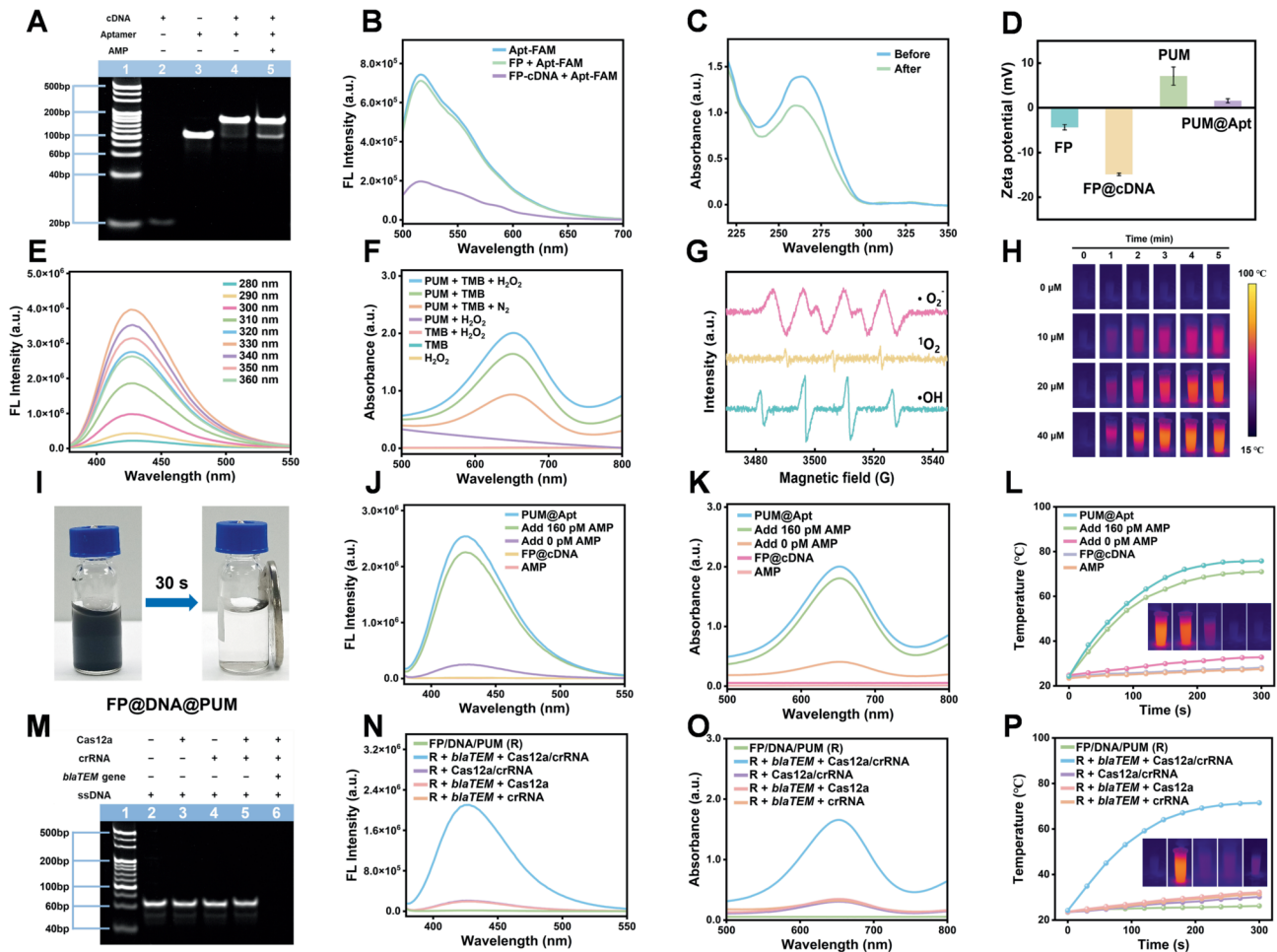


Fig. 2 (A) 12% native PAGE analysis. Lane M, marker; lane 1, cDNA; lane 2, aptamer; lane 3, cDNA + aptamer; lane 4, cDNA + aptamer + AMP. (B) Fluorescence spectra of Apt-FAM, Apt-FAM + FP and Apt-FAM after incubated with the FP-cDNA. (C) The change of UV-vis absorbance of P-Apt at 260 nm in the supernatant before and after the interaction of P-Apt with PUM. (D) Zeta potential values of FP, FP@cDNA, PUM, PUM@Apt. (E) PUM fluorescence emission spectra at different excitation wavelengths (280–360 nm). (F) UV-vis spectra of different reaction systems, PUM + H₂O₂ + TMB, PUM + TMB, PUM + H₂O₂, H₂O₂ + TMB, TMB and H₂O₂. (G) EPR spectra of PUM + H₂O₂ with DMPO/TEMP as spin trapping agent. (H) Photothermal images of the solutions under the irradiation of 808 nm of NIR light with different concentration of oxTMB (0, 10, 20, 40 μM). (I) Macroscopic characterization of magnetic properties of FP@DDA@PUM. (J) The feasibility of AMP fluorescence detection. (K) The feasibility of AMP colorimetric detection. (L) The feasibility of AMP photothermal detection. (M) 12% native PAGE analysis of the ssDNA trans-cleavage ability of Cas12a. (Cas12a:10 nM, crRNA: 10 nM, *blaTEM* gene 1 nM, ssDNA: 1 μM, cleavage time: 30 min). (N) The feasibility of *blaTEM* fluorescence detection. (O) The feasibility of *blaTEM* colorimetric detection. (P) The feasibility of *blaTEM* photothermal detection

resonance (EPR) spectroscopy revealed that the catalytic mechanism behind the coloration of PUM primarily involves the generation of hydroxyl radicals, singlet oxygen, and superoxide radicals, which are responsible for the oxidative coloration of TMB (Fig. 2G) [43]. Steady-state kinetic analysis revealed superior catalytic efficiency, with apparent Michaelis-Menten constants (K_m) of 0.108 mM and 0.943 mM for H₂O₂ and TMB substrates, respectively (Figure S5). Compared with similar reports, the enzyme activity of PUM exhibited a significant advantage (Table S1). The oxidation product of TMB (oxTMB) exhibits remarkable photothermal characteristics [44]. Based on the role of PUM in the detection process, the photothermal detection of the analyte

was realized by influencing the generation of different oxTMB. Therefore, by adjusting the temperature and pH for colorimetric detection, we were able to achieve optimal performance for both colorimetric and photothermal detection. The data revealed that optimal detection was achieved at a pH of 4 and a temperature of 30°C (Figure S6). Concurrently, we investigated the temperature changes of different concentrations of oxTMB under an 808 nm near-infrared laser. Figures S7 and 2H showed that the oxTMB demonstrated concentration-dependent photothermal responsivity under 808 nm irradiation. Figure S8 showed that the laser power also had a significant effect on the temperature change. Therefore, the photothermal conversion rate of oxTMB, obtained

by irradiating a 40 μM oxTMB solution with a 0.9 W near-infrared laser, was 42.6% (Figure S9). The findings presented above demonstrate that PUM, with its fluorescence properties and POD activity, possesses the capability to achieve tri-mode detection.

The AMP detection methodology, which integrates a magnetic separation system with a signal unit, is fundamentally based on the principles of magnetic separation. As depicted in Fig. 2I, the FP@DNA@PUM system achieved rapid magnetic separation within 30 s under the influence of an external magnetic field. To systematically evaluate the magnetic separation performance, we conducted fluorescence quantification experiments using Fe_3O_4 @PDA conjugated with the cDNA chain labeled with FAM fluorophores. As demonstrated in Figure S10, temporal fluorescence intensity analysis revealed a progressive attenuation in the supernatant following magnetic separation. The system achieved equilibrium within 30 s of magnetic field application, with quantitative calculations indicating a remarkable separation efficiency of 95.7%. This kinetic suggests rapid magnetic responsiveness and near-complete phase separation capability of the nanocomposites. Therefore, the feasibility of AMP detection was verified by changes in fluorescence, colorimetry, and photothermal properties. Figure S11 shows that the influence of AMP on PUM fluorescence is nearly negligible. As shown in Fig. 2J, 2K and 2L, the fluorescence, ultraviolet, and temperature changes in the supernatant after magnetic separation were extremely significant only in the presence of AMP. This provides evidence that magnetic separation based on FP@DNA@PUM is feasible for AMP detection. Furthermore, the cleavage activity of Cas12a and the signal change based on FP@DNA@PUM magnetic separation are two key components for *blaTEM* detection. We initially employed *blaTEM* as the target to verify the feasibility of this sensor. As described in Figure S12, a fluorescence characteristic peak was observed for the reporter, the reporter gene (FAM-ssDNA-BHQ), *blaTEM* + Cas12a + reporter gene, *blaTEM* + crRNA + reporter gene, and Cas12a + crRNA + reporter gene, respectively. However, the cleavage activity of Cas12a was activated by the addition of *blaTEM* in the presence of both crRNA and the reporter, as reflected by the strong fluorescence characteristic peak in the *blaTEM* + Cas12a + crRNA + reporter mixture solution. To verify the results obtained from the fluorescence studies, PAGE gel was performed. Figure 2M illustrates that the presence of *blaTEM*, Cas12a, and crRNA is essential for the cleavage of ssDNA into shorter fragments. The result clearly indicates the potential of CRISPR/Cas12a for the quantification of *blaTEM*. On this basis, FP@DNA@PUM was employed to achieve magnetic separation and develop a sensing system (Figure S13). Concurrently, Fig. 2N, 2O and 2P illustrate that

the activation of CRISPR/Cas12a can successfully induce fluorescence, colorimetric, and photothermal changes, demonstrating that FP@DNA@PUM can be employed for tri-mode quantification of *blaTEM*.

Analytical performance for AMP

To assess the analytical capabilities of tri-mode sensing (fluorescence, colorimetric, and photothermal) for AMP detection, we systematically optimized the concentration of PUM@Apt, reaction time, and reaction temperature through fluorescence analysis. As depicted in Figure S14, the system achieved optimal performance at 0.3 mg/mL PUM@Apt concentration with 60 min incubation at 37°C. Subsequently, we evaluated the fluorescence of PUM@Apt in the supernatant after reacting with different AMP concentrations, and conducted UV-vis monitoring of the PUM + TMB + H_2O_2 mixture under the optimized conditions. In fluorescence detection, there was a gradual increase in the fluorescence intensity as the concentration of AMP increased (Fig. 3A). The change in fluorescence intensity (ΔF) at 425 nm exhibited a good linear relationship with AMP concentrations ranging from 0.5 to 160 pM, and the LOD was calculated to be 0.34 pM ($S/N=3$) (Fig. 3B). The color heatmap visualization standardized fluorescence brightness under the ultraviolet lamp for subsequent visual detection (Fig. 3C). Concurrently, we employed a variety of antibiotics, including sulfamerazine, sulfamethoxazole, chlortetracycline, oxytetracycline, tetracycline, penicillin G, amoxicillin, kanamycin sulfate, and erythromycin, to investigate the selectivity of FP@DNA@PUM. Figure 3D illustrates that only AMP induced notable alterations in fluorescence, demonstrating the remarkable specificity of the sensing platform for detecting this antibiotic. Meanwhile, with the increase in AMP concentration, the content of PUM@Apt in the solution increased, leading to a gradual increase in the absorbance of oxTMB at 652 nm (Fig. 3E). In the range of 0.5–160 pM, the change in absorbance (ΔA) at 652 nm showed a good linear relationship with AMP concentration, and the LOD was calculated to be 0.42 pM ($S/N=3$) (Fig. 3F), with solution color transitioning from colorless to blue (Fig. 3G). In photothermal detection, the highest temperature was achieved by irradiating with an 808 nm near-infrared laser for 5 min using 0.9 W (Figure S15). Therefore, under the irradiation of an 808 nm laser (0.9 W), the temperature of the reaction solution gradually increased with the increase in AMP concentration (Fig. 3I). There was a strong linear relationship between ΔT and concentration (2–160 pM), and the LOD was calculated to be 1.32 pM (Fig. 3J). At the same time, the temperature change in photothermal detection was normalized using a heat map as shown in Fig. 3K. On this basis, the data presented in Fig. 3H and 3L demonstrate that the detection of AMP

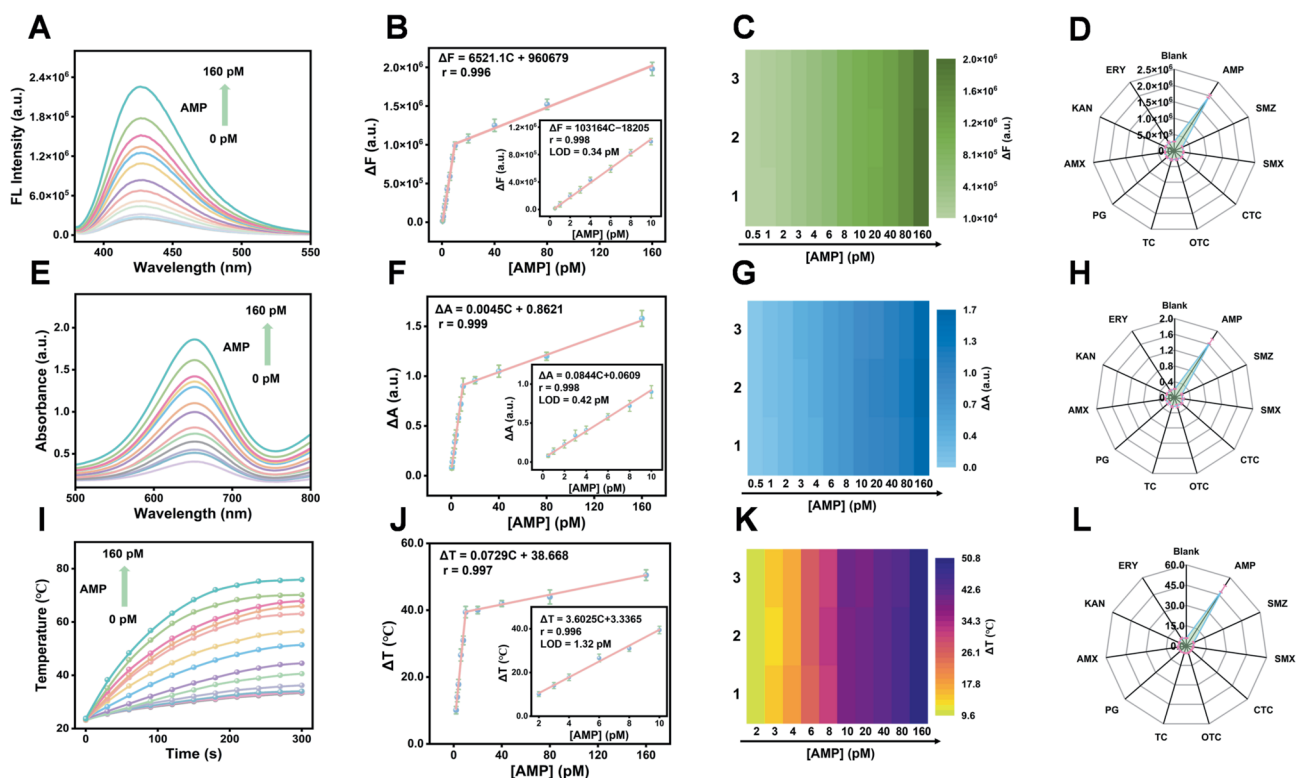


Fig. 3 (A–C) Fluorescence spectra, linear relationship, and color heatmap visualization standardized fluorescence brightness under the ultraviolet lamp with increasing AMP. (D) Selectivity of AMP fluorescence detection. (E–G) UV–vis spectra, linear relationship, and corresponding color heatmap of colorimetric with increasing AMP. (H) Selectivity of AMP colorimetric detection. (I–K) Photothermal curves, linear relationship, and corresponding color heatmap of photothermal with increasing AMP. (L) Selectivity of AMP Photothermal detection

through colorimetric and photothermal methods exhibits remarkable specificity. Simultaneously, Figures S16–S18 show that the FP@DNA@PUM-based fluorescence/colorimetric/photothermal tri-mode detection of AMP has excellent anti-interference capabilities, and the probe (FP@cDNA, PUM@Apt) exhibited excellent storage stability within 30 days at 4°C. Compared with similar AMP sensors, the tri-mode sensor based on FP@DNA@PUM exhibited extremely high sensitivity (Table S2). The findings validated that the proposed fluorescence, colorimetric, and photothermal tri-mode sensor possessed high sensitivity and specificity for AMP detection, thereby establishing a foundation for subsequent high-precision analyses using smartphones.

Analytical performance for *blaTEM*

Following AMP detection, FP@DNA@PUM was obtained via magnetic separation and introduced into a reaction system containing CRISPR/Cas12a, *blaTEM*, and crRNA. The binding of *blaTEM* to crRNA triggers the cleavage capacity of CRISPR/Cas12a to unrestricted cleavage of the single-stranded DNA component in FP@DNA@PUM, enabling the quantification of *blaTEM*. To enhance the analytical performance of *blaTEM*, the key detection factors (PUM concentration, FP@DNA@

PUM, Cas12a/crRNA ratio, and incubation shaking speed, temperature, and time) were optimized through the fluorescence signal of PUM. Figures S19A and S19B indicate that the FP@DNA@PUM nanoprobe, utilizing a PUM nanozyme concentration of 1.5 mg/mL, exhibited optimal relative activity. Subsequently, we optimized the concentration of the FP@DNA@PUM nanoprobe under identical experimental conditions. The optimal reactivity was achieved at a concentration of 2 mg/mL, which yielded the highest reactivity. The findings in Figure S19C reveal that a 1:1 ratio of Cas12a to crRNA offers the highest reaction efficiency, which was subsequently selected as the ideal reaction condition. Further investigations on the cleavage activity during Cas12a-mediated colorimetric detection indicated that the change in absorbance could reach its peak at 37°C and 1000 rpm over a period of 120 min (Figures S19D–S19F).

We systematically investigated the correlations among fluorescence responses, chromatic transitions, and thermal variations with *blaTEM* concentrations under optimized conditions to assess the potential for quantitative analysis of *blaTEM* using the developed tri-mode detection method. Figure 4A shows that the fluorescence intensity of the sensing system exhibited a concentration-dependent enhancement proportional to *blaTEM* levels.

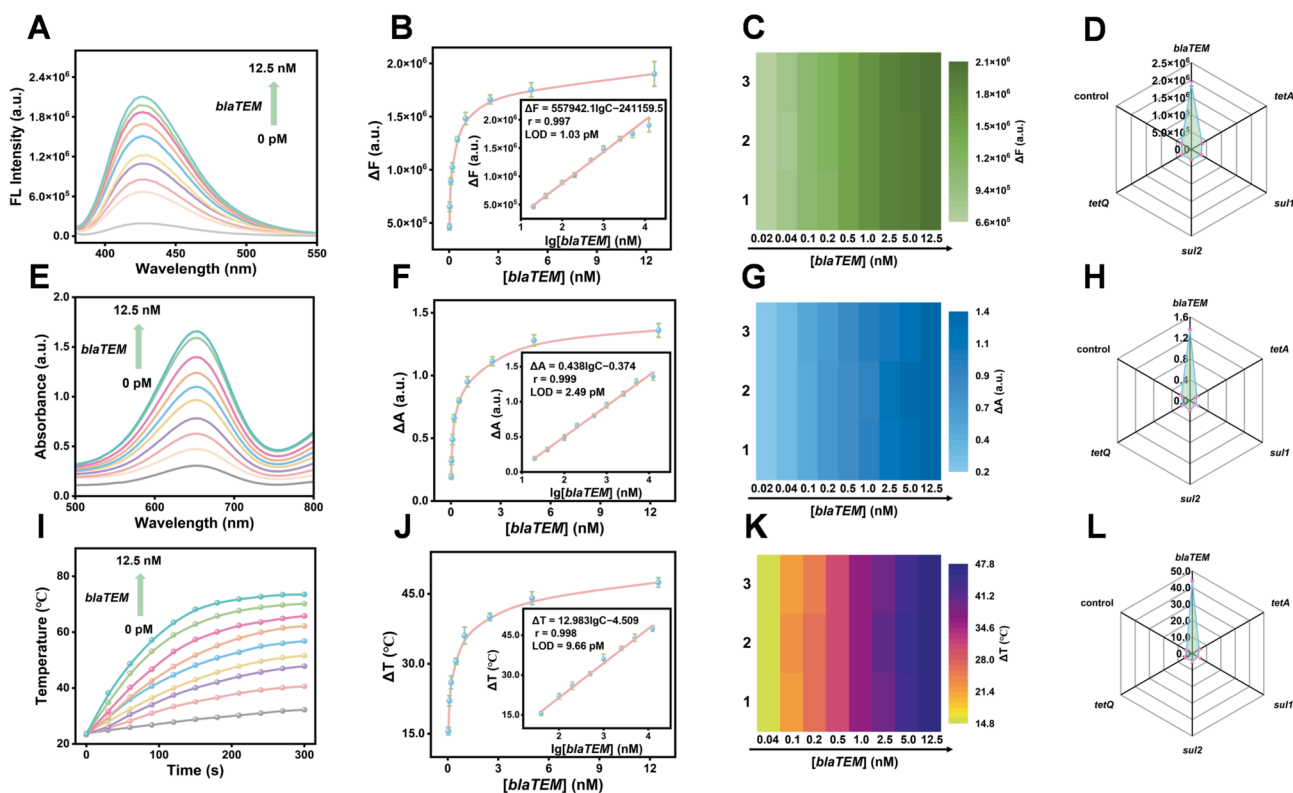


Fig. 4 (A–C) Fluorescence spectra, linear relationship, and color heatmap visualization standardized fluorescence brightness under the ultraviolet lamp with increasing *blaTEM*. (D) Selectivity of *blaTEM* fluorescence detection. (E–G) UV–vis spectra, linear relationship, and corresponding color heatmap of colorimetric with increasing *blaTEM*. (H) Selectivity of *blaTEM* colorimetric detection. (I–K) Photothermal curves, linear relationship, and corresponding color heatmap of photothermal with increasing *blaTEM*. (L) Selectivity of *blaTEM* photothermal detection

Quantitative analysis revealed a robust linear correlation between the fluorescence intensity at 425 nm and the *blaTEM* concentration (0.02–12.5 nM) (Fig. 4B). The LOD, as per the regression equation $\Delta F = 557942.1 \lg C - 241159.5$ ($r = 0.997$), can reach a value as low as 1.03 pM ($S/N = 3$). Fig. 4C displays the normalized fluorescence heatmap demonstrating a progressive chromatic intensification corresponding to enhanced fluorescence signal variation. To evaluate selectivity, we challenged the *blaTEM* sensing platform with competing resistance genes (*tetA*, *sul1*, *sul2*, *tetQ*) as potential interferents. As evidenced in Fig. 4D, exclusive recognition of *blaTEM* induced substantial signal modulation, confirming exceptional target specificity. Similarly, concentration-dependent responses were observed in both colorimetric (652 nm absorbance) and photothermal detection modes (Fig. 4E and 4I). Linear regression analysis established significant correlations between optical density/temperature variations and *blaTEM* concentration, yielding respective LODs of 2.49 pM and 9.66 pM, respectively (Fig. 4F and 4J). Furthermore, normalized heatmaps correspondingly revealed intensified chromatic signatures and thermal contrast under infrared imaging with escalating analyte levels (Fig. 4G and 4K). Meanwhile, the sensing platform represents the first time to realize the

sensing detection of *blaTEM*. Selectivity assessments employing identical resistance gene panels as colorimetric and photothermal experiments further verified the superior specificity of the biosensor (Fig. 4H and 4L). Similarly, Figures S19–S22 demonstrate that the CRISPR/Cas12a sensing platform based on FP@DNA@PUM exhibits excellent resistance to interference from *blaTEM* resistance genes and superior storage stability of probes (FP@cDNA, PUM@Apt).

Smartphone-Assisted sensing platform for visual detection of AMP and *BlaTEM*

Smartphone-assisted visual detection is an advanced and promising diagnostic tool, facilitating rapid quantitative analysis of target analytes and providing the capacity for immediate, equipment-independent detection on-site. Considering the exceptional stability, sensitivity, specificity, and excellent reproducibility of FP@cDNA and PUM@Apt, the development of a kit for the detection of AMP residues and the long-term monitoring of drug resistance gene abundance presents a promising prospect.

As schematically illustrated in Fig. 5A, the analytical workflow comprises two integrated phases. Phase I involves sequential incubation of FP@cDNA and

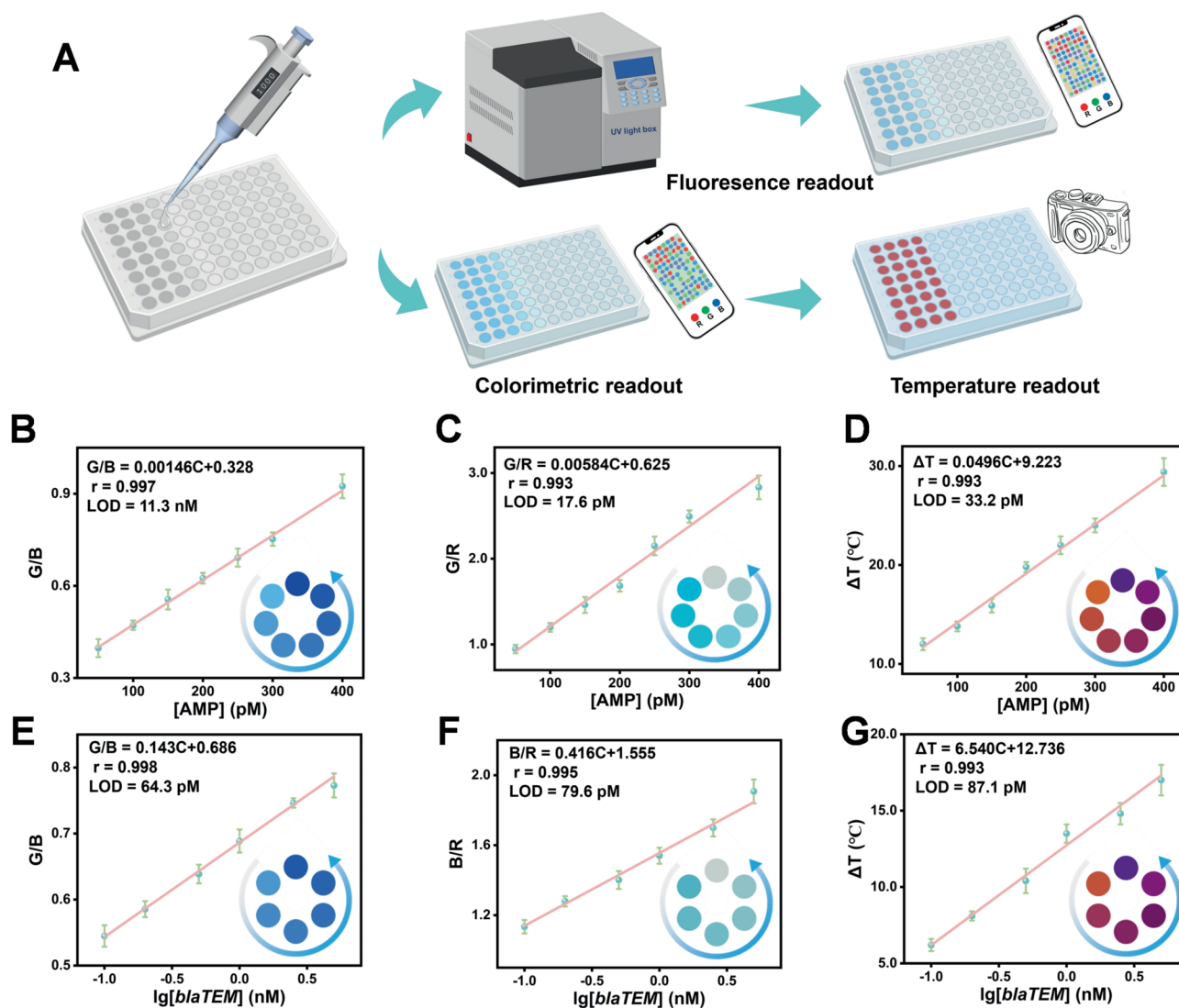


Fig. 5 (A) Schematic illustration of the programmable AMP and *blaTEM* sensing platform for tri-mode visual quantitative detection. Relationship between G/B, G/R, ΔT and AMP (B–D) or *blaTEM* (E–G). The inset shows the corresponding optical and thermal images

PUM@Apt with AMP solutions at varying concentrations, followed by magnetic separation and subsequent tri-modal signal acquisition (fluorescence/colorimetric/ photothermal). Phase II entails mixing the isolated FP@DNA@PUM complex with crRNA-Cas12a reaction mixture containing *blaTEM*, conducting magnetic separation after 120-minute incubation, and performing smartphone-assisted tri-mode detection on the supernatant. Quantitative relationships between RGB values/thermal variations and analyte concentrations were systematically established through this integrated platform. Figure 5B, 5C and 5D demonstrate smartphone-based optical analysis of AMP concentrations (50–400 nM range), revealing significant correlations between RGB chromatic shifts/thermal responses and analyte levels, achieving a detection limit of 11.3 nM. Correspondingly, Figs. 5E–5G exhibit linear detection of *blaTEM* across

0.1–5 nM concentrations with a remarkable LOD of 64.3 pM through RGB/thermal signal quantification. Notably, the platform not only realizes the integrated detection of AMP and *blaTEM*, but also provides signal cross-validation through the triple signal reading, thereby ensuring high-precision and reliable determination of AMP and *blaTEM*.

Detection of AMP and *BlaTEM* in real samples

To validate the practical reliability and analytical accuracy of our integrated sensing platform, we conducted recovery experiments using environmental water samples and bacterial resistance. As depicted in Table S3, the recovery rates of AMP spiked in environmental water samples ranged between 95.3–101.8%. The recovery rate of *blaTEM* spiked detection of *Pseudomonas aeruginosa* was between 98.6 and 101.8% (Table S4). Notably,

all relative standard deviation (RSD) values in tri-mode detection remained below 8.1%. Therefore, the proposed AMP and *blaTEM* integrated sensing platform demonstrates satisfactory recoveries and acceptable RSD values, underscoring its significant potential in the field of simultaneous visual detection of actual samples.

Conclusions

To sum up, we employed a secondary programming strategy of cDNA and Apt chains, innovatively incorporating CRISPR/Cas12a cleavage sites into the cDNA strand while embedding substrate-specific recognition regions into the Apt chain. This dual-functional engineering was accomplished while preserving the structural integrity of their complementary pairing regions, culminating in the construction of a magnetically controlled tri-mode signal amplification platform. The integrated system successfully demonstrated, for the first time, the high-precision simultaneous detection and on-site visual analysis of AMP and *blaTEM*. The magnetic separation unit was created through the covalent coupling of FP and NH₂-cDNA, while the signal transduction unit was engineered by linking P-Apt to PUM via a Zr-O-P bond. Both functional modules exhibited exceptional stability during a 30-day storage experiment. The results confirmed that the sequence-specific recognition capability of the CRISPR/Cas12a system, coupled with the target-binding selectivity of the aptamer, ensures detection specificity. Importantly, the PUM nanozyme, with POD activity and fluorescence characteristics, significantly enhances the accuracy and reliability of the sensing platform through signal cross-validation. Furthermore, this modular platform allows for easy adaptation to various antibiotic-resistance gene pairs through sequence substitution in the Apt recognition domains and CRISPR targeting sequences, demonstrating the feasibility of constructing a universal detection platform. This provides a technical foundation for the development of portable detection kits, meeting critical needs in monitoring antibiotic contamination and drug resistance transmission in the environment.

Supplementary Information

The online version contains supplementary material available at <https://doi.org/10.1186/s12951-025-03454-3>.

Supplementary Material 1

Author contributions

Tao Zhang: Conceptualization, Methodology, Validation, Formal analysis, Visualization, Software, Writing - original draft, Writing - Review & Editing. Guilin Liu: Software, Validation, Writing - original draft. Siwei Sun: Investigation, Validation, Software, Formal analysis. Zongwu Meng: Software, Validation, Formal analysis, Data Curation. Yuzhe Qiu: Formal analysis, Data Curation. Ping Ding: Supervision, Project administration, Funding acquisition, Writing - Review & Editing.

Funding

This work was supported by the National Natural Science Foundation of China (grant number 82373635), and Graduate Research Innovation Program of Central South University (grant number 2025ZZTS0167).

Data availability

No datasets were generated or analysed during the current study.

Declarations

Ethical approval

Ethics is not applicable for this work. This work does not involve human and animal ethics.

Consent for publication

All authors of this work participated in and completed the work, have read the manuscript and have agreed to publish it.

Competing interests

The authors declare no competing interests.

Author details

¹Xiangya School of Public Health, Central South University, Changsha, Hunan 410078, China

²Hunan Provincial Key Laboratory of Clinical Epidemiology, Changsha, Hunan 410078, PR China

³School of Stomatology, Fudan University, Shanghai 200030, China

Received: 30 January 2025 / Accepted: 6 May 2025

Published online: 14 May 2025

References

- Nag P, Sadani K, Mohapatra S, Mukherji S, Mukherji S. Evanescent wave optical Fiber sensors using enzymatic hydrolysis on nanostructured polyaniline for detection of β -Lactam antibiotics in food and environment. *Anal Chem*. 2021;93:2299–308.
- Behere MJ, Shinde AH, Haldar S. Determination of antibiotic resistance profile of bacterial community from environmental water using antibiotic-resistant bacterial contamination detection (ABCD) kit. *Biosens Bioelectron*. 2023;221:114943.
- Chen Y, Yang J, Zeng L, Zhu M. Recent progress on the removal of antibiotic pollutants using photocatalytic oxidation process. *Crit Rev Environ Sci Technol*. 2022;52:1401–48.
- Zainab SM, Junaid M, Xu N, Malik RN. Antibiotics and antibiotic resistant genes (ARGs) in groundwater: A global review on dissemination, sources, interactions, environmental and human health risks. *Water Res*. 2020;187:116455.
- De La Fuente-Nunez C, Cesaro A, Hancock REW. Antibiotic failure: beyond antimicrobial resistance. *Drug Resist Updates*. 2023;71:101012.
- Lu W, Guo Y, Yue Y, Zhang J, Fan L, Li F, et al. Smartphone-assisted colorimetric sensing platform based on molybdenum-doped carbon Dots nanozyme for visual monitoring of ampicillin. *Chem Eng J*. 2023;468:143615.
- Ioannou-Ttofa L, Raj S, Prakash H, Fatta-Kassinos D. Solar photo-Fenton oxidation for the removal of ampicillin, total cultivable and resistant *E. coli* and ecotoxicity from secondary-treated wastewater effluents. *Chem Eng J*. 2019;355:91–102.
- Bush K. Beta-lactamase inhibitors from laboratory to clinic. *Clin Microbiol Rev*. 1988;1:109–23.
- Wang Z, Zhang P, Ding X, Wang J, Sun Y, Yin C, et al. Co-delivery of ampicillin and β -lactamase inhibitor by selenium nanocomposite to achieve synergistic anti-infective efficiency through overcoming multidrug resistance. *Chem Eng J*. 2021;414:128908.
- Ding Y, Li Z, Xu C, Qin W, Wu Q, Wang X, et al. Fluorogenic probes/inhibitors of β -Lactamase and their applications in Drug-Resistant Bacteria. *Angew Chem Int Ed*. 2021;60:24–40.
- Jia B, Baek JH, Lee JK, Sun Y, Kim KH, Jung JY, et al. Expanding the β -Lactamase family in the human Microbiome. *Adv Sci*. 2024;11:2403563.

12. Zhang Y, Hassan MM, Rong Y, Liu R, Li H, Ouyang Q, et al. A solid-phase capture probe based on upconversion nanoparticles and inner filter effect for the determination of ampicillin in food. *Food Chem.* 2022;386:132739.
13. Lu Z, Chen S, Chen M, Ma H, Wang T, Liu T, et al. Trichromatic ratiometric fluorescent sensor based on machine learning and smartphone for visual and portable monitoring of Tetracycline antibiotics. *Chem Eng J.* 2023;454:140492.
14. Zhuang Q, Zeng C, Mu Y, Zhang T, Yi G, Wang Y. Lead(II)-triggered aggregation-induced emission enhancement of adenosine-stabilized gold nanoclusters for enhancing photoluminescence detection of nabam—disodium ethylenebis(dithiocarbamate). *Chem Eng J.* 2023;470:144113.
15. Mao Y, Shisler JL, Nguyen TH. Enhanced detection for antibiotic resistance genes in wastewater samples using a CRISPR-enriched metagenomic method. *Water Res.* 2025;274:123056.
16. Tang Q, Chen H, Diao B, Qin Z, Shao H, Zhang R, et al. PCR-free and visual detection of antibiotic resistance gene in feces genome of aquatic products by coupling CuO nanoparticles concatemers-Au@Fe₃O₄ and 3D DNA walker based on a portable blue light gel imager. *Chem Eng J.* 2024;499:156311.
17. Tao T, Wei X, Ye Z, Zong B, Li Q, Mao S. Dual recognition Strategy-Based transistor sensor array for ultrasensitive and Multi-Target detection of antibiotics. *Adv Funct Mater.* 2025;35:2413485.
18. Li H, Xie Y, Chen F, Bai H, Xiu L, Zhou X, et al. Amplification-free CRISPR/Cas detection technology: challenges, strategies, and perspectives. *Chem Soc Rev.* 2023;52:361–82.
19. Fan X, Gao Z, Ling D, Wang D, Cui Y, Du H, et al. The dCas9/crRNA linked immunological assay (dCLISA) for sensitive, accurate, and facile drug resistance gene analysis. *Biosens Bioelectron.* 2025;273:117147.
20. Fan W, Guo L, Qu Y, Zhuang Q, Wang Y. Copper-crosslinked carbon Dot hydrogel nanozyme for colorimetric - tert-butylhydroquinone biosensing and smartphone-assisted visual ratiometric assay. *J Hazard Mater.* 2024;468:133795.
21. Sastry C. New spectrophotometric methods for the determination of di-*t*-butyl hydroquinone. *Food Chem.* 1993;46:101–3.
22. Kim SH, Woo H-C, Kim MH. Solid-phase colorimetric sensing probe for bromide based on a tough hydrogel embedded with silver nanoprisms. *Anal Chim Acta.* 2020;1131:80–9.
23. Li X, Zhu H, Liu P, Wang M, Pan J, Qiu F, et al. Realizing selective detection with nanozymes: strategies and trends. *TRAC Trends Anal Chem.* 2021;143:116379.
24. Wang K, Meng X, Yan X, Fan K. Nanozyme-based point-of-care testing: revolutionizing environmental pollutant detection with high efficiency and low cost. *Nano Today.* 2024;54:102145.
25. Zheng L, Jiang Y, Huang F, Wu Q, Lou Y. A colorimetric, photothermal, and fluorescent triple-mode CRISPR/cas biosensor for drug-resistance bacteria detection. *J Nanobiotechnol.* 2023;21:493.
26. Luo X, Huang G, Bai C, Wang C, Yu Y, Tan Y, et al. A versatile platform for colorimetric, fluorescence and photothermal multi-mode glyphosate sensing by carbon Dots anchoring ferrocene metal-organic framework nanosheet. *J Hazard Mater.* 2023;443:130277.
27. Chen R, Chen X, Zhou Y, Lin T, Leng Y, Huang X, et al. Three-in-One multifunctional nanohybrids with colorimetric magnetic catalytic activities to enhance immunochromatographic diagnosis. *ACS Nano.* 2022;16:3351–61.
28. Duan N, Chang Y, Su T, Zhang X, Lu M, Wang Z, et al. Generation of a specific aptamer for accurate detection of Sarafloxacin based on fluorescent/colorimetric/sers triple-readout sensor. *Biosens Bioelectron.* 2024;249:116022.
29. Meng Z, Zhang T, Zhang Z, Qu X, Wang B, Qiu Y, et al. Multi-metal MOF-on-MOF metal-organic gel-based visual sensing platform for ultrasensitive detection of Chlortetracycline and D-penicillamine. *Biosens Bioelectron.* 2025;271:117012.
30. Chen M, Long Z, Dong R, Wang L, Zhang J, Li S, et al. Titanium incorporation into Zr-Porphyrinic Metal–Organic frameworks with enhanced antibacterial activity against Multidrug-Resistant pathogens. *Small.* 2020;16:1906240.
31. Wang X, Zang X, Wang X, Zhang W, Fang Y, Cui B. Molecularly imprinted electrochemiluminescence-colorimetric dual-mode sensor based on Mn@NC nanozyme amplification for the detection of Phoxim. *Chem Eng J.* 2024;500:156817.
32. Song Y, Liu W, Mu X, Zhong X, Cui A, Sun Y, et al. Photothermal-enhanced peroxidase-like activity of CDs/PBNPs for the detection of Fe³⁺ and cholesterol in serum samples. *Microchim Acta.* 2022;189:30.
33. Yin Y, Ren Y, Lu J, Zhang W, Shan C, Hua M, et al. The nature and catalytic reactivity of UiO-66 supported Fe₃O₄ nanoparticles provide new insights into Fe-Zr dual active centers in Fenton-like reactions. *Appl Catal B.* 2021;286:119943.
34. Jiang Y, Yang Z, Tong F, Zhang S, Zhu L, Wang L, et al. Two birds with one stone: an enzyme-regulated ratiometric fluorescent and photothermal dual-mode probe for organophosphorus pesticide detection. *Biosens Bioelectron.* 2023;224:115074.
35. Chen Y, Xia Y, Liu Y, Tang Y, Zhao F, Zeng B. Colorimetric and electrochemical detection platforms for Tetracycline based on surface molecularly imprinted polyionic liquid on Mn₃O₄ nanozyme. *Biosens Bioelectron.* 2022;216:114650.
36. Taghdisi SM, Danesh NM, Nameghi MA, Ramezani M, Alibolandi M, Abnous K. An electrochemical sensing platform based on ladder-shaped DNA structure and label-free aptamer for ultrasensitive detection of ampicillin. *Biosens Bioelectron.* 2019;133:230–5.
37. Yee BJ, Shafiqah NF, Mohd-Naim NF, Ahmed MU. A CRISPR/Cas12a-based fluorescence aptasensor for the rapid and sensitive detection of ampicillin. *Int J Biol Macromol.* 2023;242:125211.
38. Fan P, Qian X, Li Q, Jiang P, Wu Q, Huang G, et al. A novel label-free dual-mode aptasensor based on the mutual regulation of silver nanoclusters and MoSe₂ nanosheets for reliable detection of ampicillin. *Anal Chim Acta.* 2023;1251:340997.
39. Yang W, Feng L. Mg²⁺-promoted high-efficiency DNA conjugation on polydopamine surfaces for aptamer-based Ochratoxin A detection. *Anal Chim Acta.* 2024;1298:342382.
40. Lee H, Rho J, Messersmith PB. Facile conjugation of biomolecules onto surfaces via mussel adhesive protein inspired coatings. *Adv Mater.* 2009;21:431–4.
41. Lee H, Dellatore SM, Miller WM, Messersmith PB. Mussel-Inspired surface chemistry for multifunctional coatings. *Science.* 2007;318:426–30.
42. Liu M, Li X, Zhou S, Men D, Duan Y, Liu H, et al. Ultrasensitive detection of Mycotoxins using a novel single-Atom, CRISPR/Cas12a-Based nanozymatic colorimetric biosensor. *Chem Eng J.* 2024;497:154418.
43. Zhang T, Zhuang Q, Wang Y. Copper–carbon Dot aerogel: a high-performance mimetic peroxidase and its application for versatile colorimetric bioassays. *Chem Commun.* 2022;58:12955–8.
44. Li K, Wang J, Wang J, Zheng Z, Liu X, Wang J, et al. A programmable microfluidic Paper-Based analytical device for simultaneous colorimetric and photothermal visual sensing of multiple enzyme activities. *Anal Chem.* 2024;96:12181–8.

Publisher's note

Springer Nature remains neutral with regard to jurisdictional claims in published maps and institutional affiliations.